Determination of rutile transition metal oxide (110) surface terminations by scanning tunneling microscopy contrast reversal

Tianli Feng,[1,2,3,*,†] Yang Wang,[4,*] Andreas Herklotz,[4,5] Matthew F. Chisholm,[4] Thomas Z. Ward,[4] Paul C. Snijders,[4,6,‡] and Sokrates T. Pantelides[1,2,§]

[1]*Department of Physics and Astronomy and Department of Electrical Engineering and Computer Science, Vanderbilt University, Nashville, Tennessee 37235, USA*

[2]*Center for Nanophase Materials Sciences, Oak Ridge National Laboratory, Oak Ridge, Tennessee 37831, USA*

[3]*Buildings and Transportation Science Division, Oak Ridge National Laboratory, Oak Ridge, Tennessee 37831, USA*

[4]*Materials Science and Technology Division, Oak Ridge National Laboratory, Oak Ridge, Tennessee 37831, USA*

[5]*Institute for Physics, Martin-Luther-University Halle-Wittenberg, Halle, 06120, Germany*

[6]*Department of Physics and Astronomy, The University of Tennessee, Knoxville, Tennessee 37996, USA*

(Received 27 January 2020; revised 9 November 2020; accepted 24 November 2020; published 11 January 2021)

The surfaces of rutile transition-metal oxides (TMO_2) are widely investigated for catalysis, photoelectrochemical solar cells, memristors, and supercapacitors, but their structures have remained controversial. Here we employ density functional theory to predict that a universal behavior of metallic TMO_2 surfaces, i.e., the stoichiometric TMO_2 surfaces, exhibit a contrast reversal in simulated scanning tunneling microscopy (STM) images at different scanning biases. The predictions are verified by experimental STM imaging of RuO_2(110) surfaces and this feature is shown to enable accurate determinations of the TMO_2(110) surface structures under various conditions. This work provides different insights into the electronic properties of TMO_2(110) surfaces and offers an effective method to directly map the surface structure and point defects using bias-dependent STM.

DOI: 10.1103/PhysRevB.103.035409

I. INTRODUCTION

Rutile transition-metal oxides (TMO_2), where TM = Ti, Cr, Nb Tc, Ru, Rh, Pd, Re, Os, Ir, are investigated widely for both fundamental physics and practical applications in the fields of photocatalytic water splitting [1], fuel oxidation [2–4], supercapacitors [5,6], magnetic sensors [7,8], and nonvolatile ferroelectric random-access memories [9]. Knowing the surface structure is important even for the study of bulk electronic properties, such as the Dirac Nodal Lines in RuO_2 [10–12], using angle-resolved photoemission spectroscopy, as any surface states also detected in this inherently surface sensitive measurement method need to be identified. Since most properties and functionalities are determined by the surface transition metal and oxygen atoms with incomplete coordination, the prevalent low-energy (110) surface structures have been studied extensively [13–20]. For example, it has been well-established that the TiO_2(110) surface exhibits a bulk-terminated stoichiometric surface structure where half of the Ti atoms are coordinatively unsaturated (*cus*) [same as Fig. 1(a)]. However, no general consensus has been reached yet on the atomic terminations and stoichiometry of many other TMO_2(110) surfaces. For example, the RuO_2(110) surface is sensitive to growth and annealing conditions. Most works suggest that it exhibits a stoichiometric surface structure similar to TiO_2 at oxygen-deficient and/or high-temperature conditions and an oxidized structure [Fig. 1(b)] at oxygen-rich and/or low-temperature conditions [17–22]. Definitive proof has been lacking as x-ray photoelectron spectroscopy has provided limited information on the two structures and scanning tunneling microscopy (STM) images have not been able to distinguish between the two since they exhibit the same pattern and periodicity [17–20], with the actual surface structure left "hidden from the eye of the experimentalist" [23]. Moreover, other phase diagrams and surface structures were recently predicted theoretically, leaving open the question which surface structure is stable at ambient conditions [23–26].

In this paper, we combine density functional theory (DFT) and bias-dependent STM to resolve the distinct surface structures of RuO_2 under different conditions and then extend the theoretical work to demonstrate that the structure of TMO_2(110) (TM = Cr, Nb Tc, Ru, Rh, Pd, Re, Os, Ir) surfaces can be determined by bias-dependent STM measurements. The key that brings understanding of these surfaces is a feature predicted by DFT calculations and image simulations: a universal contrast reversal that appears at a certain bias for atomic structures common on TMO_2(110) surfaces. The contrast reversal results from a competition between the geometric topography of the surface and the empty-state long-range spatial decay of *d* orbitals of the surface metal atoms [27–29]. The onset bias for the contrast reversal varies in different TMO_2 materials and surface structures. This unique feature is absent in the widely studied and well-understood

*These authors contributed equally to this work.
†Corresponding author: Fengt@ornl.gov
‡Corresponding author: Snijderspc@ornl.gov
§Corresponding author: Pantelides@vanderbilt.edu

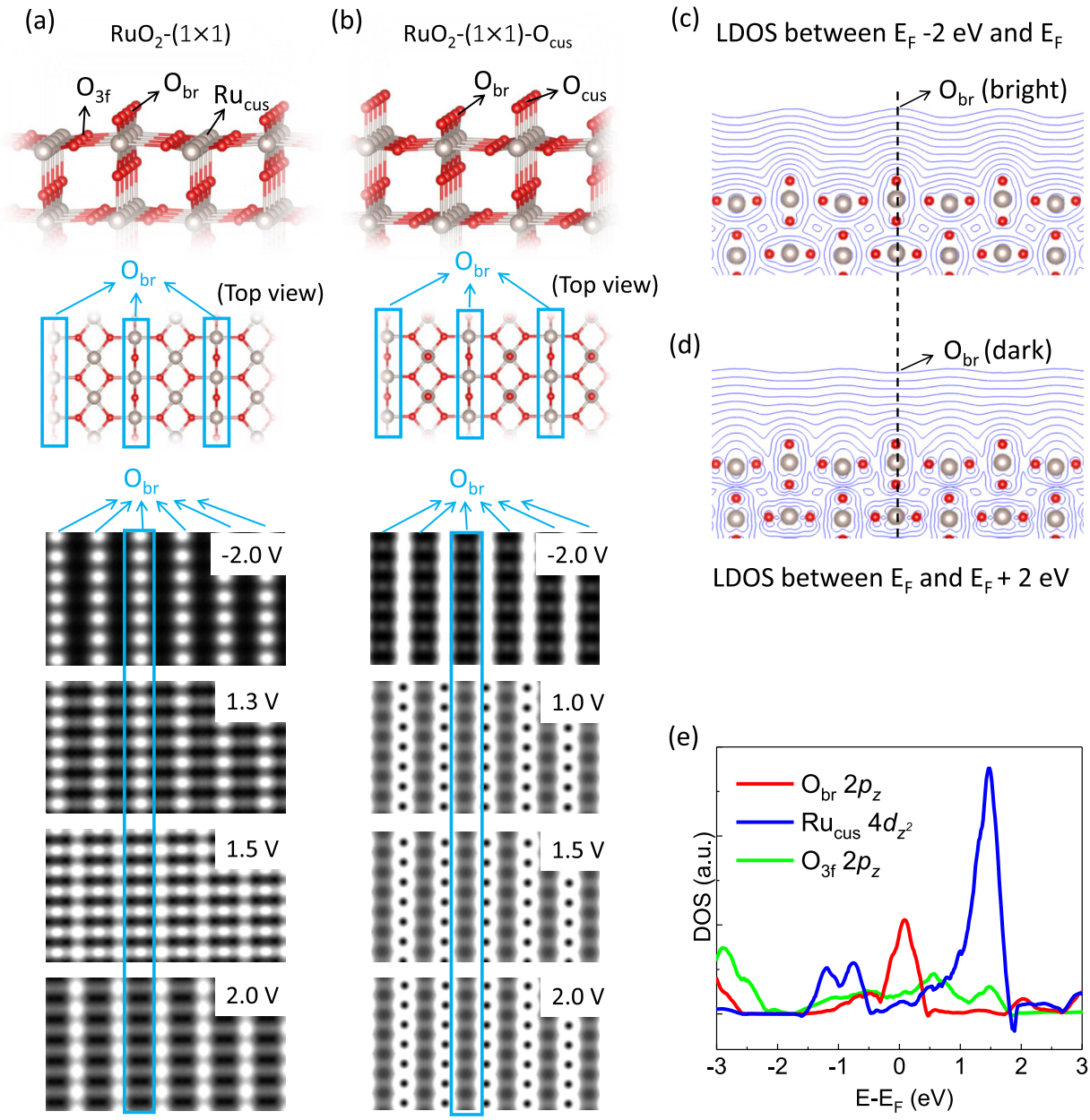

FIG. 1. First-principles predicted bias-dependent STM images, charge densities, and density of states of two possible $RuO_2(110)$ surfaces. (a) RuO_2-(1×1) surface. (b) RuO_2-(1×1)-O_{cus} surface. (c), (d), Contours showing the geometric progression of charge density for the RuO_2-(1×1) surface, with a factor of 3.16 separating neighboring contours. (c) Charge densities associated with electron states from E_F–2eV to E_F. (d) Charge densities associated with electron states from E_F to $E_F + 2$eV. (e) Site-projected density of states (pDOS) on the RuO_2-(1×1) surface atoms.

$TiO_2(110)$ surface. To test the theoretical predictions, we conducted extensive STM imaging on $RuO_2(110)$ films, which validate the predictions and clear the persisting controversies. The results show that as-grown and 653-K-annealed $RuO_2(110)$ films feature a stoichiometric RuO_2 termination, while films grown and cooled in oxygen-rich conditions feature an oxidized termination without surface reconstruction, providing a critical evaluation of theoretical predictions [23,26,30–32]. We also demonstrate that the present method, i.e., bias-dependent STM measurements, provides an effective way to directly characterize surface point defects, such as bridging-oxygen vacancies on stoichiometric RuO_2-(1×1) surfaces [17–20], which play a role in the catalytic reactivity of TMO_2 surfaces. We expect that the bias-dependent contrast reversal is common for transition metal oxide surfaces featuring exposed *d*-orbitals, and can be extended to other material surfaces in the future for broader understanding.

II. METHODS

DFT calculations were carried out using the Vienna *Ab initio* Simulation Package (VASP) [33] with the projector augmented wave method and the generalized gradient approximation of Perdew, Burke, and Ernzerhof [34] for the

electronic exchange-correlation functional. The plane-wave energy cutoff is 500 eV. The films are built by using 4 × 4 × 3 unit cells with a vacuum height of 18 Å separating the surfaces. The stoichiometric and oxygen-rich films contain 288 and 240 atoms, respectively. The total energy convergence threshold of the supercells is 1×10^{-6} eV. The lattices are relaxed with a criterion of 10^{-3} eV Å^{-1} for the forces on each atom. The electronic **k** mesh is taken as 4 × 4 × 1.

The STM images are simulated by using a constant-height method. The STM image at a bias of U is simulated by the partial charge density contrast in the electron energy range of $0 < E - E_F < U$ (if $U > 0$) or $U < E - E_F < 0$ (if $U < 0$) at a height of around 5 Å above surface TM metal atoms. The heights for different metals may differ slightly. For each material, we fix the height for various biases. We find that a change as large as 20% of the height does not change the results. In case of a band gap (e.g., TiO_2 in this work), the Fermi level is taken as the top of valence band. We acknowledge that in experiments the Fermi level of TiO_2 depends on doping, and the bias needs to be shifted by a constant to compare with our DFT simulation results.

Single crystalline RuO_2 films were grown epitaxially on rutile $TiO_2(110)$ substrates in an molecular beam epitaxy (MBE) chamber with a base pressure of 1.0×10^{-10} mbar, equipped with a laser heater for substrate heating, as well as with reflection high energy electron diffraction (RHEED). Ruthenium was deposited by physical vapor deposition using a well-outgassed electron beam evaporator. A ruthenium rod with 99.9% purity was chose as source. The growth temperature was monitored with an infrared pyrometer calibrated using a thermocouple mounted on a sacrificial substrate surface. Prior to growth, the (110) substrates (5 mm × 5 mm × 0.5 mm, CrysTec, one side polished, miscut angle <0.5°) were treated as described in Ref. [35], until an atomically flat step-and-terrace morphology was confirmed by ambient atomic force microscopy (AFM). After transfer to the MBE chamber, the $TiO_2(110)$ substrates were outgassed at ∼400 °C until the base pressure was recovered. During growth, the O_2 pressure was kept below 6.0×10^{-6}mbar. After growth, the gas was pumped out and the film was naturally cooled down to room temperature in UHV. Sample 2 was prepared at 380 °C with O_2 pressure of 1.5×10^{-5} mbar. The O_2 gas was not pumped out until the sample was cooled down to room temperature naturally. Sample 2 was further annealed in UHV at 653 K for 30 minutes after characterization, and labeled as annealed sample 2 thereafter.

The crystal structure of the prepared RuO_2 thin film was analyzed by x-ray diffraction (XRD) (PANalytical). The x-ray diffractometer is equipped with a Cu-$K\alpha$ x-ray source and mirror ($\lambda = 1.5406$ Å), which was operated at 45 kV and 40 mA. We recorded θ–2θ scans with a step size of 0.02 ° per second in a range of $2\theta = 10°$–$90°$. To eliminate the strain effect, we grow the film with thickness up to 80 nm, determined from the period of intensity oscillation in RHEED. The film crystallography is examined by θ–2θ scans and reciprocal space mapping (RSM) [36]. The θ–2θ scan reveals that the substrate (110) diffraction is accompanied by a shouldered peak at 27.9 °, which is assigned to rutile $RuO_2(110)$. The film peak is clearly separated from substrate both in horizontal and vertical directions in RSM images around (221) and (402) diffractions. The a and c lattice parameters of the film are determined as 4.511 ± 0.005 Å and 3.078 ± 0.005 Å, respectively. The as-prepared film can be considered as fully relaxed, and the subtle residual stress (if comparing to bulk lattice parameter) is probably due to thermal mismatch of the film and substrate.

STM experiments were performed in a separate UHV chamber equipped with an Omicron variable temperature STM that is connected to the MBE chamber. This setup facilitates an *in situ* STM measurement on as-grown films without exposure to the ambient. All STM images presented in this paper were taken at room temperature in the constant current mode. All experimental data described here were obtained from RuO_2 films whose structure was fully relaxed from the epitaxial lattice strain due to the lattice mismatch between the TiO_2 substrate and the RuO_2 film [36].

III. RESULTS

We take RuO_2 as the starting material in the TMO_2 group. In Figs. 1(a) and 1(b), we show schematic representations of the two most widely considered surface structures [17–20], the stoichiometric RuO_2-(1 × 1) and oxygen-rich RuO_2-(1 × 1)-O_{cus} structures, respectively. The structure in Fig. 1(a) is similar to that of the $TiO_2(110)$ surface, leaving half of the surface Ru atoms coordinatively unsaturated, labeled Ru_{cus} [2]. The outermost O atoms are bridging atoms, labeled O_{br}, and the other O atoms are threefold, labeled O_{3f}. In Fig. 1(b), the Ru_{cus} atoms that are bare in Fig. 1(a) are now covered by O adatoms, labeled O_{cus}. Using first-principles simulations, the STM images of the two different surfaces are predicted and are shown below the schematics in Figs. 1(a) and 1(b). At any single bias, the two STM images exhibit the same dark-light pattern with the same periodicity, making it impossible to distinguish between the two structures. However, as the bias changes from −2 V to +2 V, the contrast of stoichiometric RuO_2-(1 × 1) surface flips while that of the oxygen-rich RuO_2-(1 × 1)-O_{cus} does not. This surprising difference offers a clear and strong method to determine the surface structures of $RuO_2(110)$ in various oxygen pressures and temperatures. Note that the presence of such a contrast reversal on these surfaces has not been previously recognized. For example, on the surface of $TiO_2(110)$, the bridging O_{br} rows always appear as dark stripes [37].

The contrast reversal in the stoichiometric RuO_2-(1 × 1) surface can be attributed to the interplay of the lattice topography and electronic-structure effects in the STM imaging process, as shown in Figs. 1(c) and 1(d). The STM probe with a bias of −2 V follows the contours of the occupied states in between −2 eV and the Fermi level ($E_F \equiv 0$), which is dominated by the lattice topography of the surface. In this case, bridging oxygen (O_{br}) rows appear as bright stripes in the STM images since they protrude from the surface plane by a significant distance of 1.20 Å. However, when the STM probe bias increases to +2 V, it measures the contours of the empty states in between E_F and +2 eV. In this case, Ru_{cus} rows appear as bright stripes instead, since their empty states extend further in space than those of O_{br}, i.e., the empty states of Ru_{cus} are delocalized in space. Since the in-plane components of orbitals decay much faster spatially than the

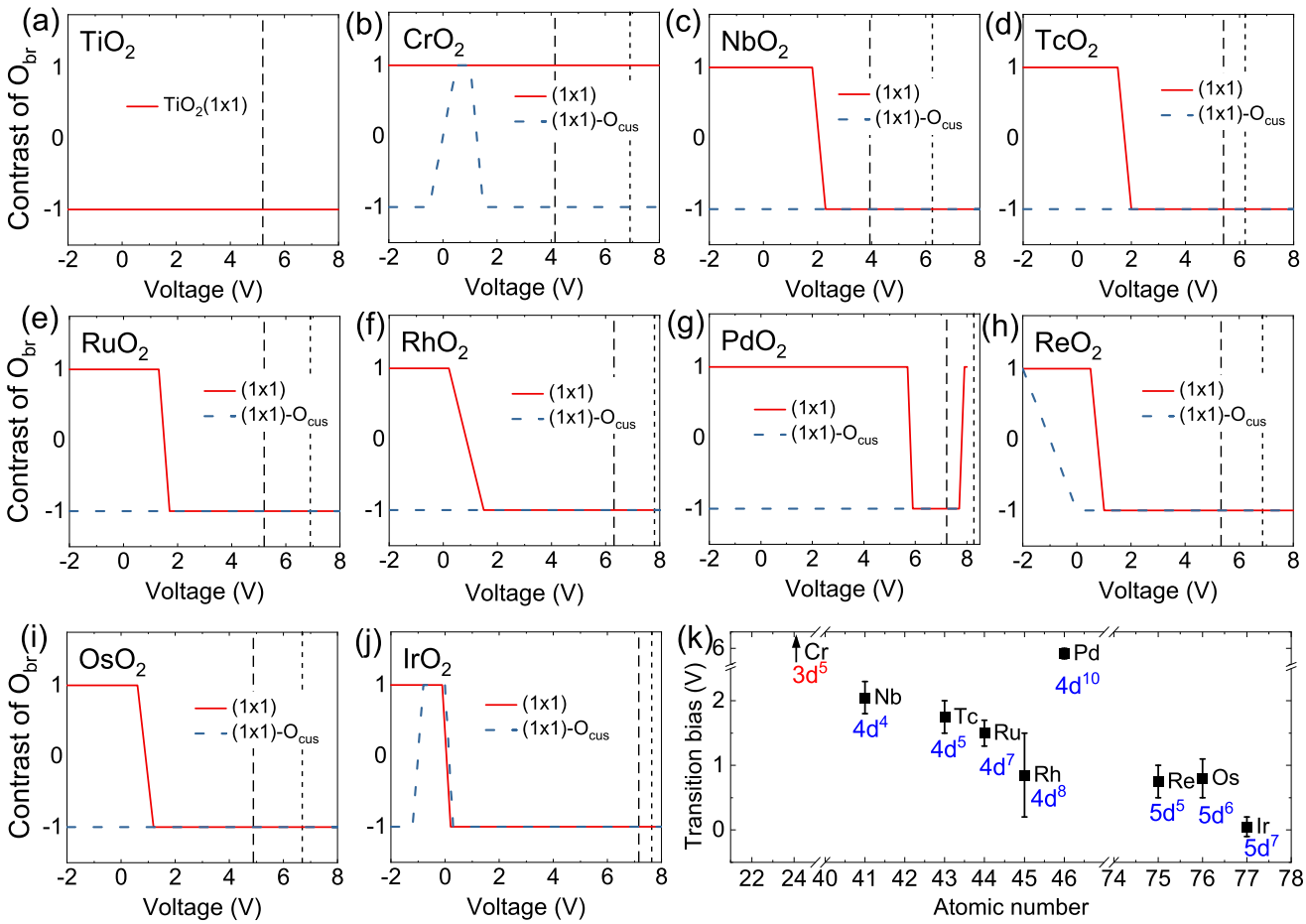

FIG. 2. First-principles predicted bias-dependent STM images of $TMO_2(110)$ surfaces. +1 and −1 represent the relative bright and dark contrasts of the O_{br} rows in STM images, respectively. Red solid and blue dashed curves represent stoichiometric TMO_2-(1×1) and oxygen-rich (1×1)-O_{cus} surface structures respectively. TiO_2 is a semiconductor, and the other TMO_2 are metallic. According to Fig. 2(a), TiO_2 is already contrast reversed in the range of bias from −2 to 8 V. (k) summarizes the onset bias of the contrast reversal of TMO_2-(1×1) surfaces as a function of atomic number of TM. Since CrO_2-(1×1) does not show contrast reversal, the bias is labeled as an upper arrow in (k). As seen in panels (c)–(j), the contrast reversals are not vertical jumps. Instead, they have finite slopes, i.e., it takes some bias range for stripes to change from fully bright (dark) to fully dark (bright). Therefore, we use error bars in (k) to account for the bias ranges for contrast reversals to complete. The work functions of the stoichiometric TMO_2-(1×1) and oxygen-rich (1×1)-O_{cus} surface structures calculated by DFT are indicated as the dashed and dotted vertical lines in each panel, respectively. The value of TiO_2 is taken from Ref. [39]. Usually, the oxygen-rich surfaces have higher work functions.

out-of-plane (z) components in vacuum above E_F, such spatial delocalization is mainly due to the $4d_{z^2}$ orbital of Ru_{cus}. As shown in Fig. 1(e), the site-projected density of states (pDOS) of the surface O_{br}, O_{3f}, and Ru_{cus} are compared to each other. The $2p_z$ orbital of O_{3f} displays a broad and nearly featureless distribution, which is undetectable in STM. In contrast, O_{br} $2p_z$ and Ru_{cus} $4d_{z^2}$ orbitals have much higher DOS, and thus govern the patterns in STM. At small negative or small positive bias, O_{br} dominates over Ru_{cus} in both electronic states and geometrical height. In general, the geometric-height effect is dominant over electronic-state effect in STM, and O_{br} appears bright. At large positive bias, the Ru_{cus}'s $4d_{z^2}$ orbital dominates over the O_{br} $2p$ orbital despite the lower geometrical height. Therefore, the contrast reversal emerges from a subtle balance between the surface geometry and the energy-dependent DOS of the orbitals relevant for tunneling [38].

With the d_{z^2} orbital spatial delocalization and the resulting STM contrast reversal found in TMO_2-(1×1) we examine all the other rutile metallic TMO_2-(1×1) surfaces (TM = Cr, Nb, Tc, Rh, Pd, Re, Os, and Ir). It is found that all stoichiometric TMO_2-(1×1) surfaces studied in this work exhibit an STM contrast reversal at a certain bias voltage, except for TiO_2 and CrO_2 as shown in Fig. 2. The detailed bias-dependent STM images of the eight materials are shown in the Supplemental Material Figs. S1–S8 [36]. Figure 2(k) summarizes the reversal onset biases of stoichiometric TMO_2-(1×1) surfaces and a general decreasing trend of the onset bias with the atomic number is found. In Fig. 2(k), we do not show TiO_2 because it is a semiconductor and does not show a contrast reversal, while all the others are metallic. We note that PdO_2-(1×1) is an exception as its reversal bias, 6 V, is much higher than the others (0∼2 V). It is clear that Pd

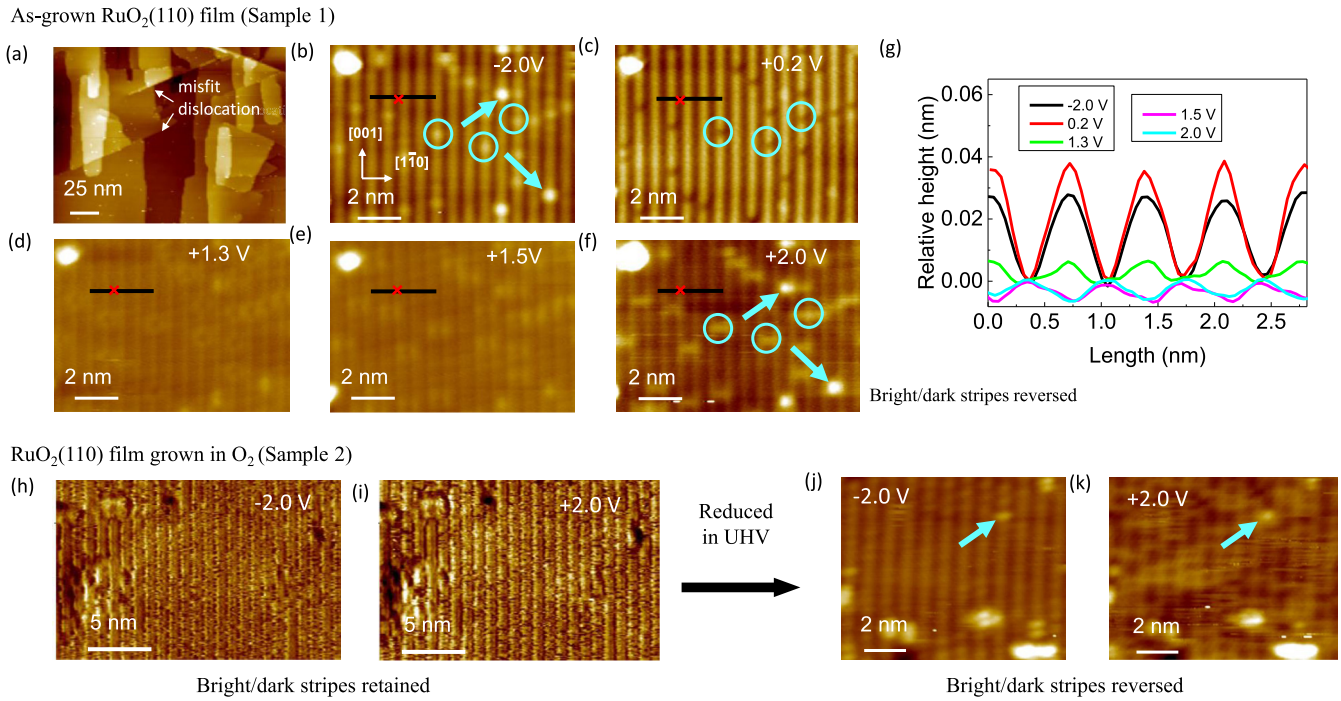

FIG. 3. Measured bias-dependent STM images of $RuO_2(110)$ films from −2 to +2 V. (a)– (f) As-grown $RuO_2(110)$ films cooled under vacuum from growth conditions. Red crosses are shown as reference points to guide eyes. The cyan arrows highlight defects which appear as bright spots for all biases and can be used as positional markers. The cyan circles highlight some defects which change contrast with changing biases. (g) Line profiles recorded perpendicular to the stripes at different bias voltages. (h),(i) $RuO_2(110)$ film grown and cooled in O_2 atmosphere. (j),(k), O_2-grown $RuO_2(110)$ film annealed (reduced) in UHV.

does not obey the trend in Fig. 2(k). This might be a result of some complex interplay between various mechanisms that are captured by the DFT calculations.

To distinguish TMO_2-(1 × 1) from TMO_2-(1 × 1)-O_{cus}, we have also simulated the bias-dependent STM contrast of TMO_2-(1 × 1)-O_{cus} surfaces, as compared in Fig. 2. Most TMO_2-(1 × 1)-O_{cus} surfaces do not show contrast reversal, as expected, since the surface TM atoms are all covered by O and the STM contrast is dominated by the lattice topography which does not depend on bias. Therefore, the outmost O_{cus} rows always show a dominance in STM images compared to the lower O_{br} rows. Interestingly, some exceptions are observed, i.e., the TMO_2-(1 × 1)-O_{cus} exhibits contrast reversal for TM = Cr, Re, and Ir. In these materials, the $2p_z$ pDOS of the O_{br} atoms are significantly higher than that of O_{cus} atoms, leading to a stronger spatial delocalization in certain energy windows near E_F (Figs. S9–S11 [36]). Nevertheless, these onset biases of TMO_2-(1 × 1)-O_{cus} are different from those of TMO_2-(1 × 1), except IrO_2. In other words, for all TMO_2 except IrO_2, the two surface structures exhibit distinct onset biases for contrast reversal while increasing the bias and, aided by simulations, can be distinguished in experimental bias-dependent STM images. For IrO_2, the transition bias is different at −1 V, which can be used to distinguish the two surfaces if the STM reversal at −1 V can be observed experimentally. As most of the TMO_2 surface structures are still unexplored [7,9,30–32,40], we expect the present method will provide important guidance in the future.

To examine the first-principles predictions and clear the controversy about the surface structures of RuO_2 films under various conditions, we conduct experimental STM measurements on different $RuO_2(110)$ samples with various biases, which have not been reported before. In this work, different $RuO_2(110)$ samples are prepared by growing films at elevated temperature using MBE, followed by three different cool-down procedures.

The first sample is as-grown (see Methods for details) at 673 K with oxygen pressure of 6×10^{-6} mbar. After growth, the oxygen is evacuated, and the sample is cooled to room temperature in a vacuum environment of around 2×10^{-9} mbar. As shown in a wide-area STM image [Fig. 3(a)], the surface is atomically flat consisting of step and terrace features. The as-prepared film is fully relaxed. A high-resolution STM image, acquired on the terrace area, displays a well-ordered structure composed of alternating high and low stripes (chains) along the [001] direction (Fig. S13 [36]). The periodicities perpendicular and parallel to these stripes are 0.66 nm and 0.31 nm, respectively. These periodicities are consistent with a (1 × 1) unit cell and agree well with the XRD measurements for the in-plane parameters. A selected area is scrutinized using dual-bias mode scanning, with the tunneling current set at 500 pA. By switching the sign of the sample bias from positive to negative in the forward and backward scanlines, respectively, we obtained the bias-dependent STM images from −2 V to +2 V with a step size of 100 mV. Representative images are rearranged following the increasing of sample bias and shown in Figs. 3(b)–3(f)

(Fig. S14 [36] for full collection of images). All images feature alternating bright and dark stripes. The contrast reversal at +1.4 V observed in Fig. 3(f) demonstrates a precise experimental validation of the DFT predictions described in Fig. 1(a). This reversal can be seen clearly in the bias-dependent line profiles recorded perpendicular to the stripes shown in Fig. 3(g). The point defects, which appear as bright spots, are used as position markers which mark the relative position change of bright and dark stripes. We also note that the point defects are also observed to exhibit bias-dependent characteristics.

To further test the DFT predictions on the role of surface oxygen, a second sample is cooled in oxygen atmosphere after growth, instead of vacuum (see Methods). As shown in Figs. 3(h)–3(i), the STM images exhibit the same pattern and periodicity as found in Sample 1. However, they do not show contrast reversal from −2 to +2 V. Finally, the second sample was annealed in UHV at 653 K for 30 min [36]. Contrast reversal of the STM images with the same periodicity is observed again [Figs. 3(j)–3(k)]. These observations are consistent with the DFT results for RuO_2-(1 × 1)-O_{cus} and RuO_2-(1 × 1) structures while experimentally demonstrating oxygen termination control.

Combining with DFT predictions, we are able to identify the surface terminations of the three RuO_2(110) films. Since the surface structure of RuO_2 can be changed under different environmental conditions (temperature and partial pressure of oxygen) [17–20], in addition to the stoichiometric RuO_2-(1 × 1) and oxidized RuO_2-(1 × 1)-O_{cus} structures discussed above, we need to consider two other plausible structures [23–25] as shown in Figs. 4(a) and 4(b), i.e., half-oxidized Ru_8O_{17}-(1 × 2) and reconstructed RuO_4(2 × 1)-tetrahedra surfaces, respectively. Based on DFT simulations, the first structure can be easily excluded since it shows a twofold periodicity that was not seen in experimental STM images. The second shows isolated spots in DFT simulations, which can also be excluded since STM images show stripes instead of spots. Therefore, we can conclude that the as-grown RuO_2(110) film surface termination is the stoichiometric RuO_2-(1 × 1) structure and the films grown in oxygen-rich conditions have the oxidized RuO_2-(1 × 1)-O_{cus} structure. Annealing in UHV can reduce the oxidized RuO_2-(1 × 1)-O_{cus} to the stoichiometric RuO_2-(1 × 1) structure. These results can be further examined by other additional techniques such as quantitative low-energy electron diffraction [41], x-ray photoelectron diffraction [42], or noncontact AFM [43].

To ensure the absence of contamination or Ti/Ru mixing in the samples, we conducted scanning tunneling electron microscopy (STEM) measurements. The Z-contrast STEM images with high resolution (Fig. S16) show that the RuO_2 film is continuous, smooth, and that there is no appreciable intermixing of Ti and Ru. The atomic flatness on the surface is well conserved during specimen preparation, as seen in Fig. S16. The outmost Ru atoms align in the same fashion as those in bulk, which is consistent with the stoichiometric RuO_2-(1 × 1) termination. Here caution should be taken. The STEM experiment involves a capping process that may modify the surface structure, and thus STEM imaging is not to rule out possible reconstructions.

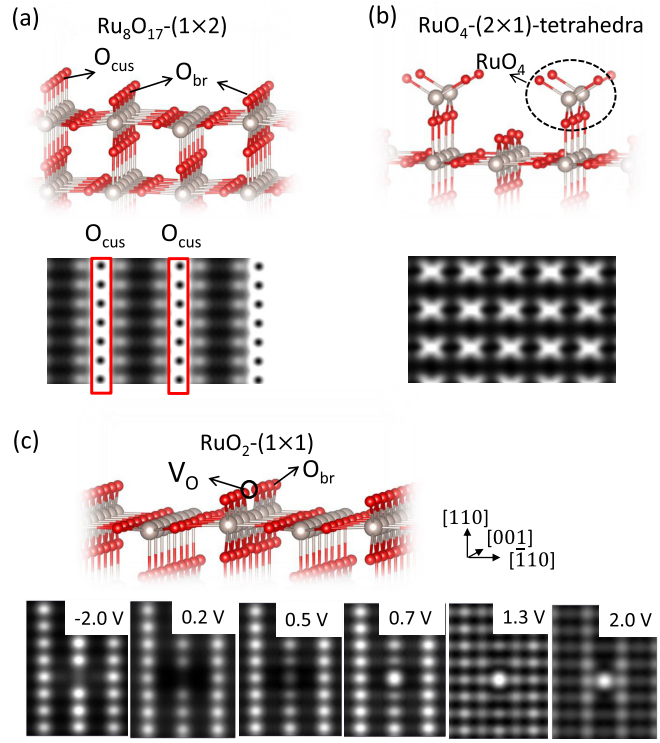

FIG. 4. First-principles calculated STM images of other RuO_2 surfaces. (a) STM image of the twofold Ru_8O_{17} − (1 × 2) surface. (b) STM image of a reconstructed, RuO_4 − (2 × 1)-tetrahedra surface, in which RuO_2 clusters are absorbed on top of the O_{cus} atoms. (c) The bias-dependent STM images of a bridging oxygen vacancy on the stoichiometric RuO_2-(1 × 1) surface.

The bias-dependent STM images can also facilitate the determination of surface point defects, which are important active sites for adsorption and dissociation reactions of, e.g., H_2O, O_2, CO_2, and carboxylic acid. Based on the STM images (Fig. 3), we find that the stoichiometric RuO_2-(1 × 1) surface has a significant number of point defects. Some representative defects are highlighted by the cyan arrows and circles. Those highlighted by circles change contrast with changing bias and represent the most common defects on the surface. The other defects, highlighted by arrows, show bright spots for all biases. The defects mentioned before, with bias-dependent appearance, are located on the bridging O (O_{br}) rows, and thus are probably oxygen vacancies (V_O), adsorbates, such as small molecules from residue gases, or RuO_4 as shown in Fig. 4(b). Oxygen vacancies are common oxygen-deficiency driven point defects in the transition-metal oxides [18,19,44,45]. To determine the defect types, we conducted bias-dependent simulations on V_O by removing a surface O_{br} atom in a supercell of 6 × 8 × 2 unit cells. As shown in Fig. 4(c), V_O changes from dark to bright as the bias changes from 0.2 and 2 V, which agrees exactly with the experimental defects highlighted by circles in Fig. 3 (we also note that it appears as bright at −2 V mainly due to the neighboring two O_{br} atoms), indicating that the circled defects, the main defects on the surface, are most likely O vacancies at the bridge (O_{br}) sites. This observation is important for catalysis as these O_{br} atoms are the main source for

oxidization catalysis [17–20]. The other defects highlighted by cyan arrows are possibly interstitial Ru atoms on the O_{br} rows as they may protrude out and appear as bright spots for all biases. These defects may be further examined in the future.

Our results clearly reveal that despite having the same rutile crystal structure, the (110) surfaces of RuO_2 and TiO_2 are quite distinct in terms of stable surface structures as a function of oxygen chemical potential [24,46]. The stoichiometric-terminated structure is the stable termination for TiO_2(110) in a wide range of oxygen pressures and temperatures [47,48]; Ti_{cus} atoms on the surface always appear as bright protrusions in STM images, and the oxygen vacancies are bright (invisible) at positive (negative) bias. O_{br} and Ru_{cus} atoms in a stoichiometric-truncated structure show contrast reversal at + 1.3 V in STM images. Oxygen vacancies appear as dark depressions between −0.2 V and +1.3 V. Beyond this bias window, they appear as bright spots. These findings provide a practical guideline for characterizing the RuO_2(110) samples and investigating the interaction between molecules and the surface.

We have also estimated whether the experimental conditions (temperate and pressure) are well inside the respective stability ranges of corresponding surface terminations, or near the border. To do this, we compare the surface energies of the stoichiometric RuO_2-(1 × 1) and RuO_2-(1 × 1)-O_{cus} terminations at the temperature and pressure conditions during the samples preparation, by using the DFT calculated results from Ref. [24], and see whether their energies differ largely or not. For Sample 1 that was prepared at 673 K with oxygen pressure at 6×10^{-6} mbar and cooled at 2×10^{-9} mbar, the surface energies of the stoichiometric RuO_2-(1 × 1) and RuO_2-(1 × 1)-O_{cus} terminations are about 77 and 90 meV/Å^2, respectively. So, the stoichiometric RuO_2-(1 × 1) termination is much more favored. For Sample 2 that was prepared and cooled to room temperature at oxygen pressure at 1.5×10^{-5} mbar, the surface energies of the stoichiometric RuO_2-(1 × 1) and RuO_2-(1 × 1)-O_{cus} terminations are about 77 and 60 meV/Å^2, respectively. In this case, the RuO_2-(1 × 1)-O_{cus} termination is much more favored. To summarize, the experimental conditions are well inside the respective stability ranges of each surface terminations.

IV. CONCLUSIONS

In conclusion, we have demonstrated that the long-range spatial decay of TM *d* orbitals induce an STM contrast reversal for the TMO_2 surfaces at certain finite biases. This behavior can be utilized in characterizing the surface structures of TMO_2 films under various conditions. We also find that surface defects can present bias-dependent contrast reversal, which offers a method for mapping surface-defect types. Compared to energy spectroscopy methods that determine surface terminations by detecting the binding energy, the methods described in this work enable the direct mapping of real-space surface species, which will provide opportunities to correlate theoretically modeled predictions to real-world experimental observations.

DOE will provide public access to these results of federally sponsored research in accordance with the DOE Public Access Plan [49].

ACKNOWLEDGMENTS

T.F. and S.T.P. acknowledge support by Department of Energy (DOE), Office of Science, Basic Energy Sciences, Materials Sciences and Engineering Division, Grant No. DE-FG0209ER46554 and by the McMinn Endowment. T.F. also acknowledges the Professional Development Funding from Oak Ridge National Laboratory. Simulations were performed at the National Energy Research Scientific Computing Center (NERSC), a DOE, Office of Science, User Facility funded through Contract No. DE-AC02-05CH11231. Simulations also used the Extreme Science and Engineering Discovery Environment (XSEDE). Y.W., A.H., M.F.C., T.Z.W., and P.C.S. acknowledge support from the U.S. DOE, Office of Science, Basic Energy Sciences, Materials Sciences and Engineering Division. We also acknowledge fruitful discussions and help from T. Berlijn.

The authors declare no competing financial interests.

[1] M. G. Walter, E. L. Warren, J. R. McKone, S. W. Boettcher, Q. Mi, E. A. Santori, and N. S. Lewis, Solar water splitting cells, Chem. Rev. **110**, 6446 (2010).

[2] H. Over, Y. D. Kim, A. P. Seitsonen, S. Wendt, E. Lundgren, M. Schmid, P. Varga, A. Morgante, and G. Ertl, Atomic-scale structure and catalytic reactivity of the RuO_2(110) surface, Science **287**, 1474 (2000).

[3] T. R. Cook, D. K. Dogutan, S. Y. Reece, Y. Surendranath, T. S. Teets, and D. G. Nocera, Solar energy supply and storage for the legacy and nonlegacy worlds, Chem. Rev. **110**, 6474 (2010).

[4] K. Seki, Development of RuO_2/Rutile-TiO_2 catalyst for industrial HCl oxidation process, Catal. Surv. Asia **14**, 168 (2010).

[5] C. C. Hu, K. H. Chang, M. C. Lin, and Y. T. Wu, Design and tailoring of the nanotubular arrayed architecture of Hydrous RuO_2 for next generation supercapacitors, Nano Lett. **6**, 2690 (2006).

[6] C. N. Chervin, A. M. Lubers, K. A. Pettigrew, J. W. Long, M. A. Westgate, J. J. Fontanella, and D. R. Rolison, Making the most of a scarce platinum-group metal: Conductive ruthenia nanoskins on insulating silica paper, Nano Lett. **9**, 2316 (2009).

[7] C. A. Ventrice, D. R. Borst, H. Geisler, J. Van Ek, Y. B. Losovyj, P. S. Robbert, U. Diebold, J. A. Rodriguez, G. X. Miao, and A. Gupta, Are the surfaces of CrO_2 metallic? J. Phys. Condens. Matter **19**, 315207 (2007).

[8] B. Deng, X. Q. Shi, L. Chen, and S. Y. Tong, Preserving half-metallic surface states in CrO_2: Insights into surface reconstruction rules, Phys. Rev. B **97**, 165404 (2018).

[9] K. Kato, Y. Abe, M. Kawamura, and K. Sasaki, Preparation of RhO_2 thin films by reactive sputtering and their characterizations, Jpn. J. Appl. Phys., Part 1 **40**, 2399 (2001).

[10] V. Jovic, R. J. Koch, S. K. Panda, H. Berger, P. Bugnon, A. Magrez, K. E. Smith, S. Biermann, C. Jozwiak, A. Bostwick, E. Rotenberg, and S. Moser, Dirac nodal lines and flat-band surface state in the functional oxide RuO_2, Phys. Rev. B **98**, 241101(R) (2018).

[11] X. Xu, J. Jiang, W. J. Shi, V. Süß, C. Shekhar, S. C. Sun, Y. J. Chen, S.-K. Mo, C. Felser, B. H. Yan, H. F. Yang, Z. K. Liu, Y. Sun, L. X. Yang, and Y. L. Chen, Strong spin-orbit coupling and dirac nodal lines in the three-dimensional electronic structure of metallic rutile IrO_2, Phys. Rev. B **99**, 195106 (2019).

[12] J. N. Nelson, J. P. Ruf, Y. Lee, C. Zeledon, J. K. Kawasaki, S. Moser, C. Jozwiak, E. Rotenberg, A. Bostwick, D. G. Schlom, K. M. Shen, and L. Moreschini, Dirac nodal lines protected against spin-orbit interaction in IrO_2, Phys. Rev. Mater. **3**, 064205 (2019).

[13] R. Schaub, P. Thostrup, N. Lopez, E. Lægsgaard, I. Stensgaard, J. K. Nørskov, and F. Besenbacher, Oxygen Vacancies as Active Sites for Water Dissociation on Rutile $TiO_2(110)$, Phys. Rev. Lett. **87**, 266104 (2001).

[14] S. Tan, Y. Ji, Y. Zhao, A. Zhao, B. Wang, J. Yang, and J. G. Hou, Molecular oxygen adsorption behaviors on the rutile $TiO_2(110) - 1 \times 1$ surface: An *in situ* study with low-temperature scanning tunneling microscopy, J. Am. Chem. Soc. **133**, 2002 (2011).

[15] J. Lee, D. C. Sorescu, and X. Deng, Electron-induced dissociation of CO_2 on $TiO_2(110)$, J. Am. Chem. Soc. **133**, 10066 (2011).

[16] C. Aguilera, J. C. González, A. Borrás, D. Margineda, J. M. González, A. R. González-Elipe, and J. P. Espinós, Preparation and characterization of CrO_2 films by low pressure chemical vapor deposition from CrO_3, Thin Solid Films **539**, 1 (2013).

[17] S. Wendt, A. P. Seitsonen, and H. Over, Catalytic activity of $RuO_2(1\ 1\ 0)$ in the oxidation of CO, Catal. Today **85**, 167 (2003).

[18] H. Over and M. Muhler, Catalytic CO oxidation over ruthenium—bridging the pressure gap, Prog. Surf. Sci. **72**, 3 (2003).

[19] H. Over, A. P. Seitsonen, E. Lundgren, M. Schmid, and P. Varga, Direct imaging of catalytically important processes in the oxidation of CO over $RuO_2(110)$, J. Am. Chem. Soc. **123**, 11807 (2001).

[20] M. Rössler, S. Günther, and J. Wintterlin, Scanning tunneling microscopy of the $RuO_2(110)$ surface at ambient oxygen pressure, J. Phys. Chem. C **111**, 2242 (2007).

[21] Y. D. Kim, A. P. Seitsonen, and H. Over, The atomic geometry of oxygen-rich Ru(0001) surfaces: Coexistence of (1×1)O and $RuO_2(110)$ domains, Surf. Sci. **465**, 1 (2000).

[22] G. Rizzi, M. Sambi, A. Magrin, and G. Granozzi, An x-ray photoelectron diffraction structural characterisation of epitaxial ultrathin $RuO_2/TiO_2(110)$ films obtained by decomposition of Ru3(CO)12, Surf. Sci. **454–456**, 30 (2000).

[23] H. A. Zakaryan, A. G. Kvashnin, and A. R. Oganov, Stable reconstruction of the (110) surface and its role in pseudocapacitance of rutile-like RuO_2, Sci. Rep. **7**, 10357 (2017).

[24] K. Reuter and M. Scheffler, Composition, structure, and stability of $RuO_2(110)$ as a function of oxygen pressure, Phys. Rev. B **65**, 035406 (2001).

[25] K. Reuter and M. Scheffler, Composition and structure of the $RuO_2(110)$ surface in an O_2 and CO environment: Implications for the catalytic formation of CO_2, Phys. Rev. B **68**, 045407 (2003).

[26] C. Xu, Y. Jiang, D. Yi, H. Zhang, S. Peng, and J. Liang, Prediction on the surface phase diagram and growth morphology of nanocrystal ruthenium dioxide, J. Am. Ceram. Soc. **97**, 3702 (2014).

[27] J. M. MacLeod, R. H. Miwa, G. P. Srivastava, and A. B. McLean, The electronic origin of contrast reversal in bias-dependent STM images of nanolines, Surf. Sci. **576**, 116 (2005).

[28] H. Mönig, M. Todorović, M. Z. Baykara, T. C. Schwendemann, L. Rodrigo, E. I. Altman, R. Pérez, and U. D. Schwarz, Understanding scanning tunneling microscopy contrast mechanisms on metal oxides: A case study, ACS Nano **7**, 10233 (2013).

[29] P. Ranjan, I. Kaplan-Ashiri, R. Popovitz-Biro, S. R. Cohen, L. Houben, R. Tenne, M. Lahav, and M. E. van der Boom, Metallic nanocrystal ripening on inorganic surfaces, ACS Omega **3**, 6533 (2018).

[30] K. Reuter and M. Scheffler, First-principles kinetic Monte Carlo simulations for heterogeneous catalysis: Application to the CO oxidation at RuO_2, Phys. Rev. B **73**, 045433 (2006).

[31] H. Wang and W. F. Schneider, Effects of coverage on the structures, energetics, and electronics of oxygen adsorption on $RuO_2(110)$, J. Chem. Phys. **127**, 064706 (2007).

[32] A. Kiejna, G. Kresse, J. Rogal, A. De Sarkar, K. Reuter, and M. Scheffler, Comparison of the full-potential and frozen-core approximation approaches to density-functional calculations of surfaces, Phys. Rev. B **73**, 035404 (2006).

[33] G. Kresse and J. Hafner, Ab initio molecular dynamics for liquid metals, Phys. Rev. B **47**, 558 (1993).

[34] J. P. Perdew, K. Burke, and M. Ernzerhof, Generalized Gradient Approximation Made Simple, Phys. Rev. Lett. **77**, 3865 (1996).

[35] Y. Wang, S. Lee, P. Vilmercati, H. N. Lee, H. H. Weitering, and P. C. Snijders, Atomically flat reconstructed rutile TiO2(001) surfaces for oxide film growth, Appl. Phys. Lett. **108**, 091604 (2016).

[36] See Supplemental Material at http://link.aps.org/supplemental/10.1103/PhysRevB.103.035409 for the STM details of the annealed Sample 2; bias-dependent STM images of all eight materials; DFT calculated charge density contours and density of states of oxygen-rich CrO_2, ReO_2, and $IrO_2(110)$ surface; XRD and reciprocal space mapping (RSM) of as-grown $RuO_2(110)$ films; STM images of the surface of as-grown $RuO_2(110)$ film; experimental STM image on the surface of annealed Sample 2; experimental STEM images of Sample 2.

[37] U. Diebold, J. F. Anderson, K.-O. Ng, and D. Vanderbilt, Evidence for the Tunneling Site on Transition-Metal Oxides: $TiO_2(110)$, Phys. Rev. Lett. **77**, 1322 (1996).

[38] U. Diebold, The surface science of titanium dioxide, Surf. Sci. Rep. **48**, 53 (2003).

[39] A. Borodin and M. Reichling, Characterizing $TiO_2(110)$ surface states by their work function, Phys. Chem. Chem. Phys. **13**, 15442 (2011).

[40] T. Joshi, T. R. Senty, P. Borisov, A. D. Bristow, and D. Lederman, Preparation, characterization, and electrical properties of epitaxial NbO_2 thin film lateral devices, J. Phys. D **48**, 335308 (2015).

[41] M. Blanco-Rey, J. Abad, C. Rogero, J. Méndez, M. F. López, E. Román, J. A. Martín-Gago, and P. L. de Andrés, LEED-IV study of the rutile $TiO_2(110) - 1 \times 2$ surface with a Ti-interstitial added-row reconstruction, Phys. Rev. B **75**, 081402(R) (2007).

[42] A. Atrei, B. Cortigiani, and A. M. Ferrari, Epitaxial growth of TiO_2 films with the rutile (110) structure on Ag(100), J. Phys. Condens. Matter **24**, 445005 (2012).

[43] M. Setvín, M. Wagner, M. Schmid, G. S. Parkinson, and U. Diebold, Surface point defects on bulk oxides: Atomically-resolved scanning probe microscopy, Chem. Soc. Rev. **46**, 1772 (2017).

[44] C. Y. Fan, J. Wang, K. Jacobi, and G. Ertl, The oxidation of CO on $RuO_2(110)$ at room temperature, J. Chem. Phys. **114**, 10058 (2001).

[45] Y. D. Kim, A. P. Seitsonen, S. Wendt, J. Wang, C. Fan, K. Jacobi, H. Over, and G. Ertl, Characterization of various oxygen species on an oxide surface: $RuO_2(110)$, J. Phys. Chem. B **105**, 3752 (2001).

[46] Q. Wang, A. R. Oganov, Q. Zhu, and X.-F. Zhou, New Reconstructions of the (110) Surface of Rutile TiO_2 Predicted by An Evolutionary Method, Phys. Rev. Lett. **113**, 266101 (2014).

[47] R. Lindsay, A. Wander, A. Ernst, B. Montanari, G. Thornton, and N. M. Harrison, Revisiting the Surface Structure of $TiO_2(110)$: A Quantitative Low-Energy Electron Diffraction Study, Phys. Rev. Lett. **94**, 246102 (2005).

[48] E. A. Kröger, D. I. Sayago, F. Allegretti, M. J. Knight, M. Polcik, W. Unterberger, T. J. Lerotholi, K. A. Hogan, C. L. A. Lamont, and D. P. Woodruff, Photoelectron diffraction investigation of the structure of the clean $TiO_2(110)(1 \times 1)$ surface, Phys. Rev. B **75**, 195413 (2007).

[49] http://energy.gov/downloads/doe-public-access-plan.